# Viscoelastic properties of rodent mammary tumors using ultrasonic shear-wave imaging

Yue Wang[1,3] and Michael F. Insana[1,2,3]

[1]*Department of Bioengineering,* [2]*Department of Electrical and Computer Engineering*
[3]*Beckman Institute for Advanced Science and Technology*
*University of Illinois at Urbana-Champaign, Urbana, Illinois 61801*

*Email: yuewang3@illinois.edu, mfi@illinois.edu*

## Abstract

Images of tumor mechanical properties provide important insights into malignant-cell processes manifest by extracellular matrix stiffening and remodeling. This paper presents a pilot study measuring in vivo mechanical-property characteristics of rodent mammary tumors using an ultrasonic shear-wave imaging technique. Shear waves are generated by a needle inserted into the tumor of anesthetized rodents that is vibrated harmonically between 50 Hz and 450 Hz. Particle motion in the tumor associated with the radiation of cylindrical shear waves is imaged using pulsed-Doppler ultrasound techniques. Estimating the spatial gradient of shear-wave phase along the direction of propagation at frequencies in the measurement range yields shear-speed dispersion curves. Measured dispersion curves were fit to those predicted by three different rheological models to estimate the elastic and viscous coefficients of the complex shear modulus. The investigation was performed in vivo on four rat-mammary fibroadenoma tumors and five xenograph mouse-mammary carcinoma tumors. Each tumor was subsequently excised for histological imaging and composition analysis. Collagen composition was measured using hydroxyproline assays that were then correlated with mechanical measurements. The goal was to relate soft-tissue mechanical behavior to biological characteristics of tumor structures, specifically the collagenous ECM protein content. The choice of rheological model and the effects of artifacts induced by shear-wave reflections at internal tissue boundaries are carefully examined in this paper. Addressing these issues is of great importance when selecting force-excitation methods and modulus estimation method to assess intrinsic tissue properties responsible for disease-specific elastographic contrast.

**key words: viscoelastic properties, mammary tumors, shear-wave imaging**

## I. INTRODUCTION

The modified structure of extracellular matrix (ECM) proteins found near breast cancer cells provides a mechanical environment that is known to modify the course of tumor formation [1]-[3]. Many physical properties of the tumor-associated ECM are fundamentally different from those of normal tissue stroma [4]. For example, tumor stroma is typically stiffer than normal stroma; in the case of breast cancer, a high-grade ductal carcinoma is approximately 13-times stiffer than normal breast tissue as measured using quasi-static elasticity imaging methods [5]. An important current area of cancer research is to determine whether biomechanical properties of ECM can provide more specific diagnostic information about the course of cancer-related processes, and thus serve to specify appropriate therapies and monitor therapeutic responses. To achieve these goals, we strive to understand how the composition and organization of cells and their associated ECM determine the biomechanical properties of a tissue. Mammary ECM constantly undergoes remodeling, even in the healthy population, but local mechanical changes induced by a malignant process can be extreme and specific to the cancer-cell pheonotype. Since stromal ECM is a principal regulator of mechanical properties at tissue scales, ECM protein content, density, and structure, e.g., as in the fibrotic changes accompanying desmoplasia, are important biomarkers. However, disruption in interstitial fluid flow, e.g., lymph edema, and misregulation of ECM remodeling enzymes, e.g., LOX-induced[1] changes in linearized cross-linked collagen bundles and MMP-induced[2] digestion of collagen fibres, also reveal details of the cellular phenotypes involved [6]. Furthermore, these different biological effects may be evident in mechanical measurements at different force frequencies given the complex behaviors possible in biphasic tissues (solid ECM, interstitial fluids). The hope is that disease-specific changes in ECM can be safely monitored from images of mechanical properties [7].

Elasticity imaging has been developed to serve this purpose. It is used to quantify tissue mechanical properties noninvasively at the meso-scale (0.1-10 mm) and larger, utilizing phase-sensitive imaging modalities such as ultrasound, MRI and optical imaging technologies. One form of ultrasonic shear-wave imaging measures shear-wave velocities over a bandwidth of excitation-force frequencies to generate shear-wave dispersion curves. Fitting shear-wave sound speed measurements at different frequencies to the values predicted from a representative rheological model, we estimate model-based viscoelastic properties of the tissue that characterize the elastic and viscous responses to force stimuli. Several preliminary clinic studies have been conducted to quantify breast-tissue mechanical properties using shear-wave imaging methods [8], [9]. Measurements made in this manner introduce artifacts that are difficult to correct given a fairly-limited state of knowledge of soft-tissue mechanics. As we will show, measurement distortions from wave reflections bias modulus estimates in a manner that depends on the shear wavelength. Bias can also occur if the rheological model is not representative of the tissue at the force frequency of the measurement. The Kelvin-Voigt model is the current default, but recent studies suggested a role for other models [10], [11]. More

[1] Lysyl oxidase is a protein encoded by the LOX gene that normally cross links and stabilizes ECM. However it is upregulated in cancer cells where it promotes metastatic transitions.

[2] Matrix metalloproteinases (MMPs) are a family of proteins expressed by cells to degrade the ECM.

complex rheological models often require a larger number of tissue parameters to fully represent tissue dispersion curves in vivo. The quest to understand sources of elasticity contrast in soft tissues began at the University of Illinois half a century ago [12], [13], when the pioneering studies of Floyd Dunn and colleagues first inquired how tissue structure and macromolecular composition influence sound scattering and absorption. Since the long-term objective is to translate viscoelastic measurements into descriptions of ECM properties and disease states, the relationships between stromal ECM features and viscoelastic measurements – even those contaminated by measurement artifacts – must be clearly understood.

Toward this goal, we measured properties of two types of rodent mammary tumors: rat fibroadenoma and 4T1-implanted mouse carcinoma. Fibroadenoma is a benign, spontaneously-occurring tumor characterized by a hyper-proliferation of normal type I stromal collagen. The collagen fibers in the ECM matrix are assembled with hydrogen bonds that break and reform when stressed over time to give a viscoelastic response to the applied force [14]. The concentration and architecture of collagen proteins in the ECM are responsible for many mechanical properties of mammary tissues [7]. In contrast, 4T1 cells are a metastatic late-stage mammary carcinoma line. Due to high MMP secretion and other properties, 4T1 cells generate tumors with very little ECM collagen. However, the fibers that are present are highly linearized compared to the winding shape in benign fibrous tumors [15]. This fiber structure along with dense-packed cells and an altered lymphatic system increases the stiffness of these malignant mouse tumors. The two mammary tumors selected are very different from each other in biological structure – fibroadenomas contain thick braids and sheets of collagen and few cells, while the 4T1 carcinoma tumors are densely cellular with little collagen – yet both stiffen as the tumor grows.

The purpose of this study was to (a) test the reproducibility of a shear-wave imaging technique in a small cohort of in vivo rodent mammary tumors; (b) compare the measured mechanical properties of the two tumor types with their histology and collagen content to explore contrast mechanism; (c) investigate the role of rheological models in assessing the complex modulus of mammary tumors; and (d) examine the amount of measurement bias arising from boundary reflections in small tumors.

## II. METHODS

### *A. Animal models*

Benign rodent tumors: Four Sprague-Dawley female rats (Harlan, Indianapolis, IN), aged from 5 to 10 weeks, that had developed spontaneous mammary fibroadenomas of size 2 to 4 cm were used for evaluation. The tumors appeared grossly homogeneous in morphology and consisted of abundant fibrous connective tissue with a high collagen density. Manual palpation revealed a variation in stiffness among these tumors.

Malignant rodent tumors: Syngeneic orthotopic xenograft mouse tumors were induced by a late-stage metastatic mouse-mammary cancer cell line 4T1 (CRL-2539, ATCC, Manassas, VA). The tumors grew a relatively uniform morphology, characterized by a high density of cells and little ECM. 4T1 cells were stored, cultured and collected as the ATCC protocol recommended. Tumors were implanted by subcutaneous injection of $10^4$ 4T1 cells suspended in 50 ml of cell media into the $4^{th}$ or $9^{th}$ mammary pad of a normal 8-16 week-old BALB/c mouse. The injection site was monitored daily until the tumor reached 1 cm in size, when its mechanical properties were measured in vivo. Injected cells initiated tumor growth in 80% of the animals. The tumor size grew rapidly at the injection site during the first 2-3 weeks, then growth slowed as the tumor mass stiffened. Although larger tumors are easier to manipulate, image, and analyze, large tumors often formed a necrotic core. To minimize necrosis, tumors were scanned once they reached 1.0 cm in diameter.

After scanning, all tumors were excised and fixed in 10% neutral formalin prior to a hematoxylin and eosin staining process. The rat tumors were diagnosed as mammary fibroadenomas each with a different ECM content that correlated with tumor age. All mouse tumors were diagnosed with anaplastic mammary carcinoma. Diagnostic reports from a professional pathologist showed minimal difference among these tumors. The tumors were densely cellular, infiltrative with a few interspersed ingrowing capillaries. Fig 1 shows histopathologic slides of two representative mammary fibroadenomas and one representative mammary carcinoma.

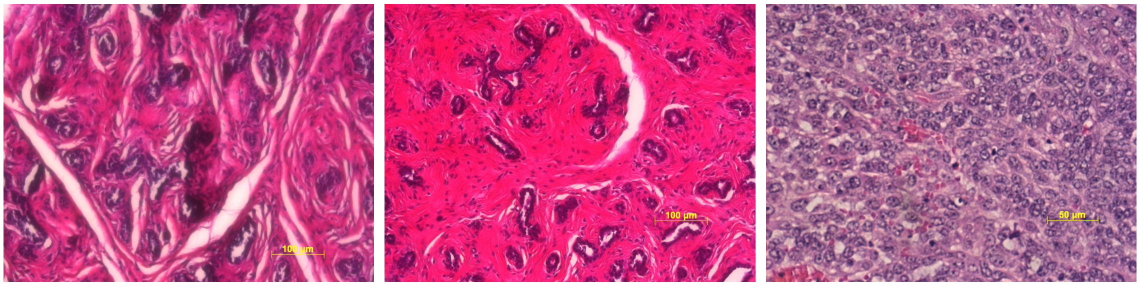

Fig. 1. Optical microscope images of H&E stained tumors. On the left is an early-in-development rat fibroadenoma tumor, and in the middle is a mature rat fibroadenoma tumor with densely packed collagen fibers (both images are at 40X). On the right is a sample from a mouse carcinoma (80X).

### B. Imaging procedure

All rodents were anesthetized before imaging with a combination of ketamine hydrochloride (87 mg/kg) and xylazine hydrochloride (13 mg/kg) under a protocol approved by the Institutional Animal Care and Use Committee at the University of Illinois. The skin of each anesthetized animal was shaved in the region around the tumor before imaging. The animal was placed on an acrylic plate in a prone position and submerged in 37 °C degassed water bath with its head above of the water surface. The water provided an acoustic window for non-contact ultrasonic scanning and thermal control during anesthesia. B-mode imaging of the tumor was performed to select a Doppler imaging plane. Then a 17-gauge stainless-steel needle was inserted vertically into the tumor under ultrasonic guidance to select the needle depth and avoid damaging large vessels. A SonixRP system (Ultrasonix Medical Corporation, Richmond, BC, Canada) was used for RF echo acquisition and B-mode imaging. An L14/38 linear-array Doppler probe scanned the tumor in a plane at a fixed scan angle of 30° relative to the needle axis [17]. The transmit focus of the ultrasound beam was set to the center of the measurement field of the tumor. The center frequency was set at 7 MHz.

A mechanical actuator vibrated the needle harmonically for 0.3 s along its long axis ($z$ axis). The acquisition sequence of the linear-array probe was synchronized to the actuator, with the pulse repetition frequency (PRF) set to 12.5 kHz in Doppler mode with a packet size of 6. The actuator vibration frequency ranged from 50 Hz to 450 Hz in increments of 50 Hz. The peak-to-peak voltage of the actuator was set to a low level (2V) to avoid needle slippage and mechanical nonlinearities, but at some cost of velocity SNR. See Fig. 2 for setup details. The tissue displacement at the needle surface was 1-9 micrometers depending on the excitation frequency and tissue stiffness.

Immediately following shear-wave data acquisition, each anesthetized animal was euthanized in a $CO_2$ tank and the tumor was excised. Parts of the tumor were fixed for histology and collagen quantification. Hydroxyproline assays were performed on three samples per tumor to measure the collagen-protein content following the assay protocol of Samuel [16]. Hydroxyproline content can be used as an indicator to determine collagen content [29].

### C. Modulus estimation

Assume each tumor is a semi-infinite, homogeneous and viscoelastic medium that supports shear-wave motion at the applied vibration frequency. In this idealized situation, shear waves radiate cylindrically in the $x, y$ plane away from the vibrating needle with a particle velocity aligned along $z$, the vibration movement axis of the needle. The $z$-axis component of particle velocity $v_z$ measured over time and along the $x$ axis (Fig. 2) is represented by

$$v_z(x,t) = Ae^{-\alpha x} \cos(\omega t - kx + \phi_0) \ ,$$

where $A$ denotes vibration amplitude and $\alpha$ is the shear-wave attenuation coefficient at radial vibration frequency $\omega$. Also, $\phi_0$ is the initial shear-wave phase and $k = \omega/c_s(\omega) + j\alpha(\omega)$ is the complex wavenumber. $c_s(\omega)$ is the speed that harmonic shear waves at frequency $\omega$ travel through tissue.

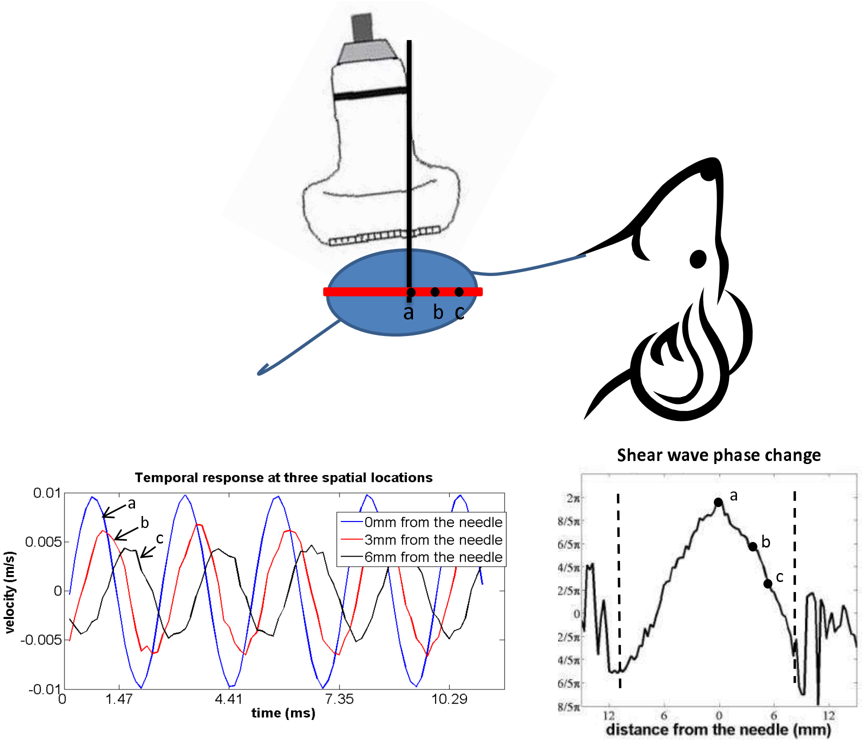

Fig. 2. In vivo setup used for ultrasonic shear wave imaging experiments. The $z$ axis is aligned along the long-axis of the needle. The $x$ axis is normal to $z$ and in the scan plan of the Doppler probe (red line in the top diagram). Lower left figure demonstrates the harmonic movement at three different locations on the tumor. Lower right figure shows the phase of the harmonic movement over the measured spatial locations at 400 Hz.

Wavenumber $k$ is estimated using a spatial-phase gradient method [18]; specifically, it is the slope found from linear-regression analysis applied to the temporal phase of particle velocity measured along a radial axis perpendicular to the needle axis. Particle velocity $v_z(t,x)$ is computed using a Doppler estimator as described previously [17]. When the assumptions of a homogeneous, semi-infinite medium are violated, the phase gradient is not constant along the radial axis $x$ (See Fig. 2).

Phase measured along the $x$ axis is conveniently estimated from the temporal Fourier coefficients of particle velocity, $\mathcal{F}_t\{v_z(t,x)\} = V_z(\omega,x)$, measured at vibration frequency $\omega$. The phase angle is $\arg(V_z) = \tan^{-1}(\Im\{V_z\}/\Re\{V_z\})$, and the phase gradient is given by the real part of the complex wavenumber,

$$\Re\{k\} = \text{argmin}_{k,b}\|\arg(V_z(\omega,x)) - (kx+b)\|^2 \, . \tag{1}$$

Dispersion curves are plots of shear speed as a function of $\omega$. For mass density $\rho$, the relationship between shear-wave speed and the complex shear modulus is well known to be [19],

$$c_s(\omega) = \omega/\Re\{k(\omega)\} = \sqrt{\frac{2(G'^{\,2} + G''^{\,2})}{\rho(G' + \sqrt{G'^{\,2} + G''^{\,2}})}}\ , \tag{2}$$

where the complex shear modulus $G = G' + jG''$ is composed of a shear storage modulus $G'$ and a shear loss modulus $G''$. $G$ is estimated using nonlinear regression to fit the predictions of Eq. (2) to the measured dispersion curves.

The Maxwell and Kelvin-Voigt (K-V) rheological models each have two parameters that describe the medium in which waves travel as continua characterized by elastic $\mu$ and viscous $\eta$ coefficients. The Maxwell model combines an elastic spring with a viscous dashpot in series to describe tissues as fluid-like media capable of stress relaxation behavior but no significant creep behavior. The K-V model is a spring and dashpot placed in parallel, which describes tissues as solids that can creep but show little stress relaxation. The corresponding complex shear moduli for the K-V and Maxwell models are, respectively [20],

$$\begin{aligned} G^K &= \mu + j\omega\eta \\ G^M &= \frac{j\omega\eta\mu}{\mu + j\omega\eta}\ . \end{aligned} \tag{3}$$

The Zener (or standard-linear) model has three-parameters, where a series spring-dashpot unit $(\mu_1, \eta)$ is placed in parallel with a second spring $\mu_2$. It is the simplest model that expresses both the stress relaxation and the creep observed in biphasic media like mammary stroma. The complex shear modulus for the Zener model is given by [20]

$$G^Z = \frac{\mu_1\mu_2 + j\omega\eta(\mu_1 + \mu_2)}{\mu_2 + j\omega\eta}\ . \tag{4}$$

We can assign $\mu = \mu_1 + \mu_2$ as the net elastic modulus and $\eta$ is the viscous coefficient when comparing model behaviors. Distinctions among these three rheological models depend on the load frequencies applied to the tissues. Below, we compare goodness-of-fit metrics for the three models at the 50-450 Hz bandwidth used in our study.

### *D. Modeling boundary artifacts*

When shear waves travel through heterogeneous tissues, which is common in vivo, the assumption that tissue is a homogeneous continuum of semi-infinite extent is violated. Tissue heterogeneities and tumor boundaries generate reflected waves and spatially-varying wave speeds that distort the linear-phase assumption and hence bias estimates of the complex shear modulus. Because shear waves are highly attenuated at frequencies above 1 kHz, reflections in a finite lesion are of concern primarily at frequencies below

1 kHz where we have made measurements. Wave reflection and shear-speed variation artifacts are easy to detect because, when they occur, the gradient of temporal shear-wave phase (Fig. 3) is not constant. The question addressed in this section is how much measurement bias is generated in the presence of a reflected wave?

A simple one-dimensional (1-D) analysis of plane-wave phase is summarized in the Appendix. The amount of bias is regulated by several factors such as the stiffness contrast between the lesion and its boundary materials, the shear wavelength, and attenuation coefficient [21]. Here we only discuss the effect of lesion size on the estimation bias. Fig. 3 shows the phase shift that is predicted in the presence of a wave reflection for $\omega/2\pi = 100$ Hz, [3]$\alpha = 0.5\ \mathrm{cm}^{-1}$, $\lambda$ = 2 cm, $A_0$ = 1, and $\phi = 0$. From the plot on the right, we can estimate the sound speed bias as the size of a spherical lesion boundary $R$ increases.

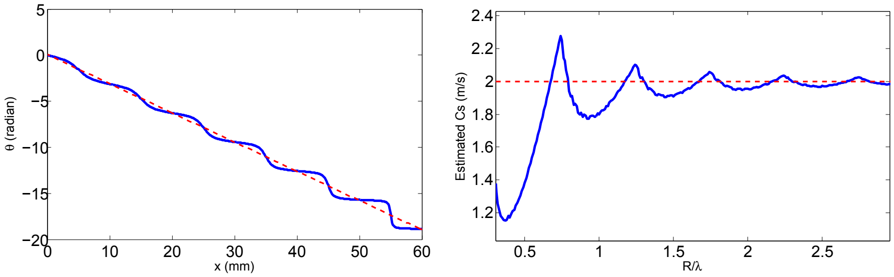

Fig. 3. The left plot shows how shear-wave phase, $\theta(x)$, varies as a function of radial distance from a source ($\omega/2\pi = 100$ Hz) placed at $x$ = 0. The result is from a 1-D simulation described in the Appendix. There is a strong reflector located at $x = R = 60$ mm from the source. The blue line is $\theta(x)$ in the presence of reflected waves and the red line ($\theta = -2\pi x/\lambda$) is the phase without reflections. Shear wave speed $c_s(\omega)$ is estimated from the slope of $\theta(x)$ over $0 \leq x \leq R$. The plot on the right shows how shear-wave speed estimates vary as the distance between the source and reflecting boundary increases. $R$ is normalized by the shear wavelength $\lambda$.

To examine other geometries, we employed a numerical simulator to generate shear-wave data so we can measure the phase bias resulting from reflections. In one situation, our finite-difference time-domain (FDTD) solver [22] was used to simulate 1-D shear waves that propagate in time along the $x$ axis, while measuring the $z$-axis component of particle velocity along $x$. The simulated medium was a homogeneous viscoelastic solid with elastic modulus $\mu = 4$ kPa and viscous coefficient $\eta = 0.1$ Pa·s. A source, located at the origin, vibrated harmonically at either 150 Hz or 250 Hz. Shear waves were computed numerically at all values of $x$ every $\Delta t = 6\ \mu$s during a 0.3 s experiment time, then down-sampled in time as needed to match data acquired during experiments. We applied the phase-gradient method described above to estimate shear-wave speed. In each plot below, the vibration plane source is at the origin and there is a perfectly

---

[3] We measured the shear attenuation coefficient in fresh excised liver to be 0.8-2 $\mathrm{cm}^{-1}$ for vibration frequencies in the range of 50-300 Hz [28]. We selected $\alpha = 0.5\ \mathrm{cm}^{-1}$ in this analysis to be conservative.

reflecting boundary located at $x = R$.

In the second situation, the FDTD solver was reconfigured to generate 3-D cylindrical waves from a needle-like source vibrating at 150 Hz and placed in the center diameter of a spherical inclusion. We measured wave phase within the stiff inclusions that were embedded in soft backgrounds. Shear waves radiating from the linear source were reflected at the sphere surface. The medium inside the sphere was homogeneous and viscoelastic with elastic modulus coefficient $\mu = 4$ kPa and viscous coefficient $\eta = 0.1$ Pa·s. The background medium surrounding the sphere was softer, with $\mu = 0.5$ kPa and $\eta = 0.1$ Pa·s. All other simulation parameters were the same as the 1-D FDTD simulations. Note that reflections in a 1-D spatial geometry are stronger than those in 3-D, so in Fig. 4 we used a smaller lesion ($R = 18$ mm radius) to illustrate the pattern of phase bias instead of using $R = 44$ mm as in the 1-D simulations.

Finally, we constructed gelatin phantoms [23] to verify experimentally a few of the simulation results. Gelatin hydrogel cylinders were constructed using 8% gelatin with different diameters. Each was embedded in a 4% gelatin-gel background that was roughly 4 times softer. Shear-wave speeds measured at 150 Hz were examined for all gelatin phantoms. A needle was inserted along the long axis of the cylinder and vibrated while shear waves were measured.

## III. RESULTS

### A. Boundary-effect simulation and experiments

Simulation results show that wave reflections generate stair-step patterns in the phase as a function of distance from the source (top row of Fig. 4). Depending on the lateral extent to which phase data are used to calculate a slope for shear-wave speed estimation, Fig. 4 shows there are different amounts of bias introduced. For example, computing the phase gradient over 40 mm of phase measurements using 1-D wave simulations results in very little measurement error compared with estimates taken over 4 mm of data. Notice for the 1-D data in the bottom row of Fig. 4 that the bias error within an 18-mm-radius sphere is larger than it is in a 44-mm-diameter sphere. Reflected-wave attenuation increases as the sphere diameter increase.

The divergence of cylindrical waves in the 3-D simulations (lower row, right) significantly reduces the variation in measurement bias error with range. The results of our data analysis applied to these 3-D wave-simulation data are summarized in Table I. Since only one frequency was simulated, we assume an elastic medium when estimating the modulus values shown.

The results of ultrasound measurements in gelatin phantoms, where the vibration source was located along the long axis of a stiff cylindrical gelatin inclusion while shear waves radiating along the axis normal to the vibration, are given in Table II.

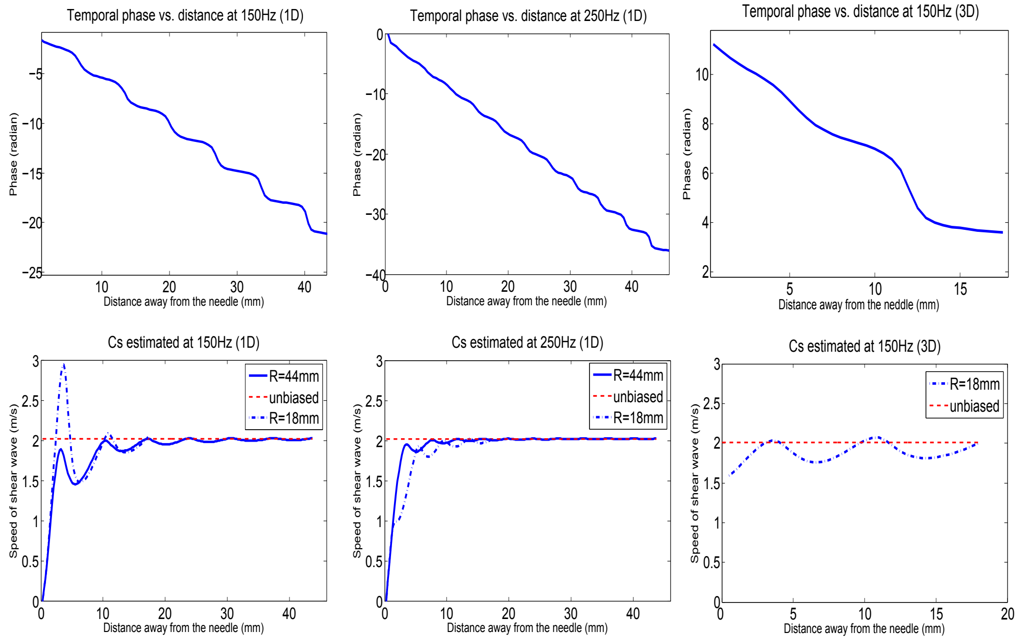

Fig. 4. Numerical simulation of shear-wave phase in the presence of reflections yielding $c_s$ measurements. Plots in the top row are shear-wave phase simulated as a function of distance from a vibrating source. There is a reflector positioned 44 mm from the source placed at the origin for the 1-D wave geometry, while the reflector is at a 18 mm radius in the data using 3-D geometry. In the bottom row, estimates of shear-wave speed are plotted as a function of source-reflector distance. $R = 18$ mm in the dotted lines and $R = 44$ mm in the solid lines. Each value in a wave-speed plot is found by applying linear regression to phase data from the origin up to the corresponding abscissa value shown. Plot columns from left to right are the 1-D FDTD simulation at 150 Hz, 1-D FDTD simulation at 250 Hz, and 3-D FDTD simulation at 150 Hz. The dotted red lines in the sound-speed plots represent the shear-wave speed input to the simulation. In all situations, speed estimates obtained from the simulated wave data converge to the values input to the simulator.

Measurements based on 3-D simulations and phantom experiments both show that reflections generated in the smallest inclusions produced the largest biases in shear-wave speed measurements. Generally, shear speed and modulus estimates in the presence of reflections are biased low. As the inclusion size increases, the modulus bias became less that 10-15% provided the inclusion diameter was greater than two shear wavelengths. These findings give us some guidance on estimating measurement bias for different size inclusions or lesions based on the shear wavelength. Of course, by increasing the vibration frequency we decrease the shear wavelength and increase the attenuation coefficient, and thus we reduce bias while increasing random errors as the echo SNR falls. Also using pulsed- rather than harmonic-force stimulation reduces reflections at the cost of reduced SNR for particle velocity estimates. There are several factors that need to be considered in assessing measurement errors.

TABLE I
SHEAR-WAVE SPEED BIAS VERSUS SPHERE DIAMETER AT 150HZ (3-D SIMULATION)

| Diameter (cm) | No. wavelengths | $c_s$ (m/s) | $\mu = c_s^2\rho$ [Pa] | $\mu$ bias |
|---|---|---|---|---|
| $\infty$ | $\infty$ | 2.089 | 4363.9 | 0.00% |
| 4 | 3 | 2.034 | 4137.2 | 5.20% |
| 2.5 | 1.88 | 2.019 | 4076.4 | 6.59% |
| 1.8 | 1.35 | 1.818 | 3305.1 | 24.26% |
| 1.2 | 0.9 | 1.612 | 2598.5 | 40.45% |

TABLE II
SHEAR-WAVE SPEED BIAS VERSUS GEL CYLINDER DIAMETER AT 150HZ (EXPERIMENT)

| Diameter (mm) | No. wavelength | $c_s$ (m/s) | $\mu = c_s^2\rho$ [Pa] | $\mu$ bias |
|---|---|---|---|---|
| 74.8 | 7 | 1.61 | 2592.1 | 0% |
| 31.3 | 2.93 | 1.61 | 2592.1 | 0% |
| 20.2 | 1.88 | 1.46 | 2131.6 | 17.77% |
| 12.7 | 1.18 | 1.38 | 1904.4 | 26.53% |
| 15.7 | 1.46 | 1.26 | 1587.6 | 38.75% |
| 10.5 | 0.98 | 1.00 | 1000.0 | 61.42% |

### *B. Mechanical properties of rat mammary fibroadenoma in vivo*

In tumor imaging experiments, shear-wave speeds at multiple frequencies were measured. Figure 5 shows shear-wave dispersion curves measured in vivo on four different rat fibroadenoma tumors. When purely elastic material was assumed and only the shear wave speed at 150 Hz was used, the elasticity of the four tumors would be 2.16, 2.34, 4.49, and 7.13 KPa. To obtain viscoelastic properties, the shear-wave speeds for each tumor were fit to a Kelvin-Voigt (K-V) rheological model to estimate the complex modulus coefficients, $\mu$ and $\eta$, via Eqs. (2), (3). Modeled curves were fit to measured data by selecting model parameters that minimized the reduced $\chi^2$ statistic,

$$\chi^2 = \frac{1}{(N-n-1)} \sum_{i=1}^{N} \left( \frac{\hat{c}_i(\omega) - c_i(\omega)}{\sigma_i(\omega)} \right)^2 , \tag{5}$$

where $N$ is the number of different frequency observations and $n$ is the number of model parameters. The best-fit model curves are plotted with the data in Fig. 5 and the modulus coefficients based on those curves are listed in Table III. Notice that the fitting equation given in Eq. (1) provides estimates of $\Re\{k\}$ and hence $\hat{c}_i$. On the other hand, Eq. (5) tells us how well the shear speed values predicted from a rheological model fits measured shear speed values used in the estimation of shear-modulus coefficients.

Tumor size information obtained from B-mode image is provided. Larger fibroadenomas generally appeared as histologically more mature tumors with denser collagen content.

We used the Maxwell model to predict dispersion curves, applied those results to the same rat tumor measurements in Fig. 6, and found the modulus coefficients listed in Table IV. Similarly, the Zener model was applied to the rat tumor measurements in Fig. 7 and the resulting modulus coefficients are listed in Table V.

Histological analysis of these tumor tissues revealed that the fibroadenomas in rats 1 and 2 were in the early stage of development (Fig. 1 left, where the tissue is less fibrotic and the ducts retain a normal shape). Conversely, the lesions in rats 3 and 4 were at the latter stage of fibroadenoma development (Fig. 1 middle, where there is more dense fibrosis and the ducts have collapsed).

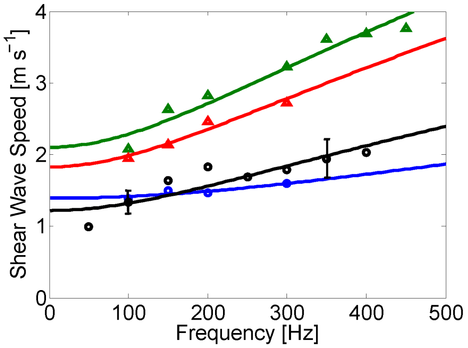

Fig. 5. Dispersion curves measured in four different rat fibroadenomas. '○' denotes the measured shear-wave speed of early stage fibroadenoma tissues and '△' denotes that of the more mature fibroadenomas. Solid lines represent the best-fit K-V model curves.

TABLE III

ESTIMATES OF SHEAR MODULUS COEFFICIENT FOR THE FOUR RAT FIBROADENOMAS IN FIG. 5 ASSUMING THE KELVIN VOIGT MODEL. THE MINIMUM REDUCED $\chi^2$ VALUES FOR THE BEST-FIT MODELS ARE GIVEN.

| rat | $\mu$ [Pa] | $\eta$ [Pa·s] | $\chi^2$ | tumor size [mm] |
|---|---|---|---|---|
| 1 | 1832.2 | 0.9 | 0.86 | 28.8 |
| 2 | 1485.6 | 1.16 | 1.52 | 30.9 |
| 3 | 2728.6 | 3.46 | 2.55 | 39.1 |
| 4 | 4420.4 | 3.54 | 1.71 | 33.3 |

### C. *Mechanical properties of mouse mammary carcinoma in vivo*

Using the same experimental procedures and data analysis, we examined in vivo the mammary carcinomas from five mice. Tumors were of different sizes. Histology revealed that tumors were composed almost entirely of cancer cells with minimum fibrotic changes. (Fig. 1 right). Fig. 8 shows the dispersion curves of the five mouse carcinomas and Table VI summarizes the mechanical parameters estimated assuming the K-V model. Tumor size information was calculated from ultrasound B-mode images.

### D. *Collagen*

The rat and mouse mammary tumors were vastly different in structure and composition. Since collagen is a cancer biomarker and the principal component of stroma

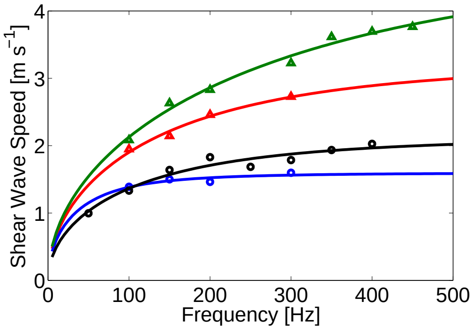

Fig. 6. Dispersion curves measured in four different rat fibroadenomas. '○' denotes the measured shear-wave speed of early stage fibroadenoma tissues and '△' denotes that of the more mature fibroadenomas. Solid lines represent the best-fit Maxwell model curves.

TABLE IV
Estimates of shear modulus coefficient for the four rat fibroadenomas in Fig. 6 assuming the Maxwell model.

| rat | $\mu$ [Pa] | $\eta$ [Pa·s] | $\chi^2$ |
|---|---|---|---|
| 1 | 2558.6 | 3.03 | 0.59 |
| 2 | 4604.0 | 1.92 | 1.25 |
| 3 | 10722.0 | 3.53 | 0.89 |
| 4 | 24453.0 | 3.99 | 0.97 |

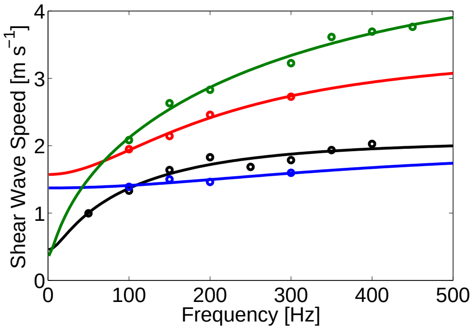

Fig. 7. Dispersion curves measured in four different rat fibroadenomas. '○' denotes the measured shear-wave speed of early stage fibroadenoma tissues and '△' denotes that of the more mature fibroadenomas. Solid lines represent the best-fit Zener model curves.

TABLE V
Estimates of shear modulus coefficient for the four rat fibroadenomas in Fig. 7 assuming the Zener model.

| rat | $\mu_1$ [Pa] | $\mu_2$ [Pa] | $\eta$ [Pa·s] | $\chi^2$ |
|---|---|---|---|---|
| 1 | 3937.4 | 3613.9 | 2.06 | 0.76 |
| 2 | 4385.0 | 217.1 | 2.34 | 1.39 |
| 3 | 11793.8 | 3127.7 | 5.01 | 1.03 |
| 4 | 23385.0 | 128.8 | 4.18 | 0.67 |

responsible for tissue viscoelastic properties, we measured the collagen content of each tumor to compare with measured mechanical properties (see Fig. 9). We found that rat fibroadenomas are in the range of 85-110 mg hydroxyproline/g dry tissue. This range overlaps values reported for human breast fibroadenoma [24], [25]. In contrast, the 4T1 mouse carcinoma model contains very little ECM collagen, generally in the range of 1-8 mg hydroxyproline/g dry tissue. Note that hydroxyproline constitutes 15% of total collagen content [29], so the collagen concentrations are roughly seven times larger than the hydroxyproline concentration values reported in Fig. 9. Hypothesis testing shows there is good correlation between modulus parameters and collagen content in both rat

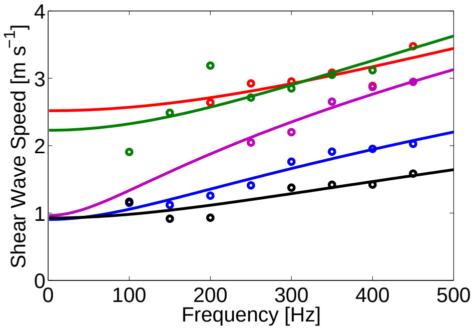

Fig. 8. Dispersion curves measured in five different mouse carcinomas. Solid lines are the best-fit K-V model curves.

TABLE VI
ESTIMATES OF SHEAR MODULUS COEFFICIENT FOR THE FIVE MOUSE CARCINOMAS IN FIG. 8 ASSUMING THE K-V MODEL.

| mouse | $\mu$ [Pa] | $\eta$ [Pa·s] | Tumor size [mm] | line color |
|---|---|---|---|---|
| 1 | 857.0 | 0.56 | 11.0 | black |
| 2 | 894.4 | 0.95 | 11.4 | blue |
| 3 | 926.9 | 1.78 | 10.5 | magenta |
| 4 | 4464.6 | 2.5 | 16.5 | green |
| 5 | 6343.1 | 2.4 | 14.1 | red |

fibroadenoma (correlation coefficient equals 0.95 for $\mu$, 0.81 for $\eta$) and mouse carcinoma (correlation coefficient equals 0.93 for $\mu$, 0.99 for $\eta$).

The spontaneous rat mammary fibroadenomas are a reasonable model for human fibroadenomas. However, the 4T1 mouse carcinoma is not human-like in structure or composition; they are composed predominantly of cells with very little fibrotic response. Nevertheless, these data give us strong evidence that the elastic shear modulus is highly correlated with collagen content.

We also note that several investigators found that collagen hydrogel stiffness was found to increase quadratically with collagen concentration in low-concentration gelatins obtained from a variety of animal sources (the data are summarized in [26]). In this study, we found that $\mu \sim C^{2.2}$ for the mouse carcinomas, as expected for low-collagen-concentration polymers. However, $\mu \sim C^{4.3}$ in the fibroadenomas, which suggests that tissues with much higher concentrations of type I collagen form complex internal structures that increase shear elastic modulus in nonlinear ways.

## E. Rheological model comparisons

The reduced $\chi^2$ statistic values reported in the tables specify the goodness of fit among the measured dispersion curves and values predicted by three rheological models. The

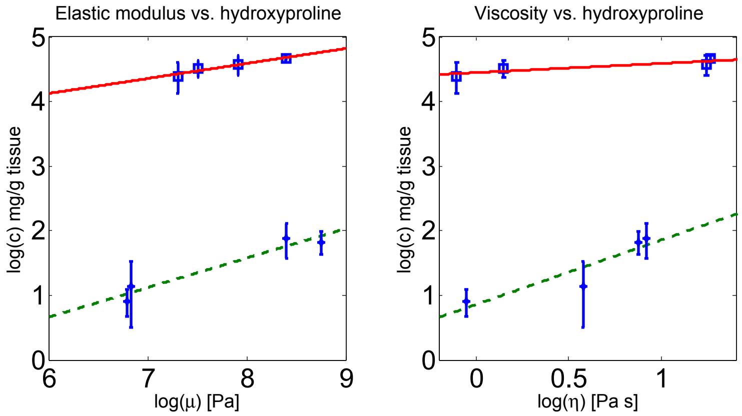

Fig. 9. The hydroxyproline concentrations measured for rat fibroadenomas are plotted on a log-log scale as a function of the corresponding tissue elastic coefficient (left) and viscous coefficient (right) in the upper curve. (Denotes by '□') The same quantities were measured for mouse carcinomas and plotted in the lower curve. (Denotes by '-')The error bar represent the standard error of collagen content from 3 independent collagen assay tests. Assuming there is a power-law relationship between the elastic modulus and hydroxyproline content of the form $C = A\mu^n$, we find $n = 0.46$ and $A$ = 0.12 mg/g for the mouse carcinomas (lower curve) and $n = 0.23$ and $A$ = 15.3 mg/g for the rat fibroadenomas. Error bars indicate one standard error. Also note that we can write $\mu = BC^m$, where $B = (1/A)^{1/n}$ and $m = 1/n$. Assuming the same power-law relationship between the viscous modulus and hydroxyproline content of the form $C = A\eta^n$, we find $n = 1.0$ and $A$ = 2.4 mg/g for the mouse carcinomas (lower curve) and $n = 0.15$ and $A$ = 85.4 mg/g for the rat fibroadenomas.

values are averaged for all data in a group and reported in Figure 10. The K-V model gives larger fitting residuals for fibroadenomas compared with the Maxwell and Zener models. However all three models fit the data from carcinomas equally well. We note that the K-V model fits the shear-wave dispersion data poorly at low frequencies where the measurement uncertainty is lowest.

## IV. DISCUSSION

The two rodent models used in this study provided us with an opportunity to study very different tumor structures, one that is dominated by fibrosis and the other by cellular hyperplasia. Human breast cancers are often heterogeneous combinations of these and other tissue types, and so we hope to learn more about how tumor structure and composition generate dynamic mechanical-feature contrast at load frequencies between 50-450 Hz by comparing these results against each other and with those of the literature.

The elastic and viscous coefficients measured for the *four rat mammary fibroadenomas* were closely correlated with lesion size and age. Also the measurement values were very different depending on the rheological models used to fit to the dispersion curve. We found $\mu = 1.8$ - 4.4 kPa and $\eta = 0.9$ - 3.5 Pa·s when the K-V model is used in modulus-coefficient estimation. The elastic and viscous coefficients for *five mouse mammary*

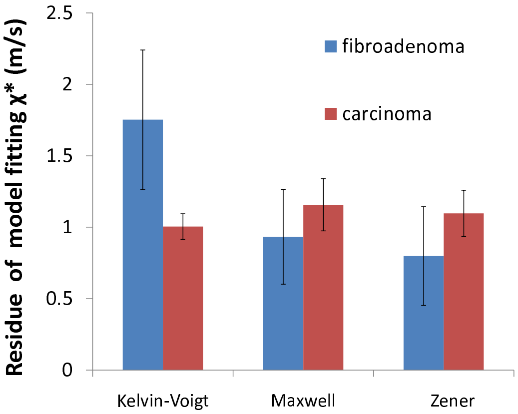

Fig. 10. Reduced $\chi^2$ statistics for the Kelvin-Voigt, Maxwell, Zener rheological models. Error bars indicate ±1 standard error.

*carcinomas* spanned the range $\mu$ = 0.9 - 6.3 kPa and $\eta$ = 0.6 - 2.4 Pa·s, respectively, for the K-V model. Some of the literature results taken from human pathological breast tissues are compared with our results in Fig. 11.

Sinkus et al. [27] applied harmonic force excitation at 65 Hz and a direct-inversion modulus estimation under K-V model assumption to compare in vivo measurements made in six human breast-fibroadenoma patients with the results from six breast-carcinoma patients. They found $\mu$ = 0.7 - 2.7 kPa and $\eta$ = 0.4 - 4.2 Pa·s for the fibroadenomas and $\mu$ = 2.6 - 3.4 kPa and $\eta$ = 0.7 - 4.6 Pa·s for the carcinomas with the lesion size not specified.

In a study by Samani et al. [5], a harmonic force at 0.1 Hz was applied using indentation methods to estimate Young's modulus in fresh ex vivo human breast tissue samples at room temperature. These investigators measured[4] $\mu$ = 2.14 ± 0.95 kPa in 16 fibroadenomas and $\mu$ = 3.47-14.1 kPa in 31 samples of infiltrating carcinomas of different grades.

Firstly, our K-V-based measurements of $\mu$ for rat fibroadenomas and mouse carcinomas are in general agreement with the human results from the literature, except that measurements for the three smallest mouse carcinomas are much lower than that for the larger two lesions (Table VI). Our simulation and phantom measurements showed that $\mu$ estimates in lesions smaller than two shear wavelengths are expected to be negatively biased because of internal shear-wave reflections. The range of $R/\lambda$ for all rat fibroadenomas is 1 – 5, but the values for the mouse carcinomas are between 0.2 – 1. We estimate that the three smallest mouse carcinomas are likely to be 3 times stiffer than the measured values because of reflected-wave artifacts. A factor of three

---

[4] Young's modulus $Y$ values were converted to shear modulus elastic coefficient $\mu$ using $\mu = Y/3$.

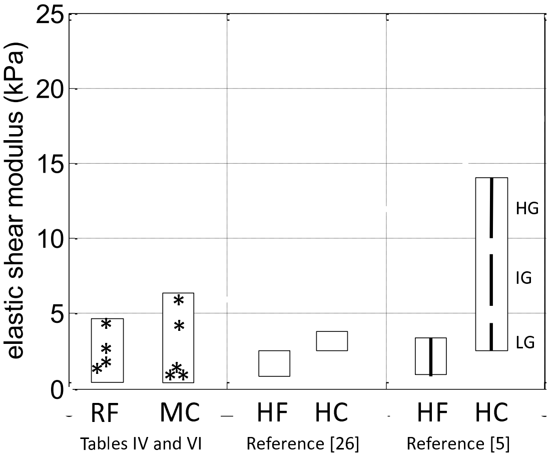

Fig. 11. Comparisons of the elastic shear modulus coefficients measured for rat fibroadenomas (RF) from Table IV and for mouse carcinoma (MC) from Table VI in this study, and for human fibroademoma (HF) and human carcinoma (HC) from [27] and [5]. In [5], infiltrating ductal carcinomas are separated into low grade (LG), intermediate grade (IG) and high grade (HG) pathology tumors. Boxes indicate the range of measurements made in a study, while lines indicate the range as the mean value ± one standard deviation.

would increase the mouse carcinomas into the range of the human IDC lesions. Using transient elastography could possibly eliminate reflection. However, the transit pulse excitation is a broad band excitation where the frequency bandwidth is governed by the impulse response of the tissue itself. Thus, sometimes, the desired frequency to avoid reflected waves might not be achieved. On the other hand, $\mu$ measurements from the two later-stage mouse carcinomas exhibit less bias, and thus fall into the range of low-grade human IDC tumors. Late-stage human carcinomas, like the 4T1 mouse cancer model, are characterized by large MMP secretions that reduce fibrosis levels. The elevated stiffness in these tumors is likely due to increased interstitial pressures (edema) that occur as hyperplasia reduces lymphatic flow [14]. If we let the mouse carcinomas grow larger, we would find a large necrotic core is likely to develop and thus these lesions would become increasingly heterogeneous.

Secondly, others [5] showed that $\mu$ values for carcinomas correlate with the histological grade. Similarly we found that the stiffness of rat fibroadenomas corresponded to the histological appearance and collagen content of the lesion. Generally speaking, the older and larger fibrotic tumors had higher shear-modulus coefficients. The collagen concentration in fibroadenomas is highly related to tumor stiffness and viscosity, with the correlation coefficients consistently $> 0.9$ between $\mu$ or $\eta$ and the collagen concentration $C$. Power-law equations predict these relationships. We found that $C = A\mu^n$, or equivalently $\mu = BC^m$, where $A, B, n, m$ are power-law coefficients and $m = 1/n$. Yang et al. [31] and other groups found that $n \sim 0.5$ ($m \sim 2$) for low-concentration collagen hydrogels. Thus doubling the collagen concentration produces a gel with four times the stiffness, $\mu$. We see from Fig. 9, that the stiffness of mouse carcinomas increases quadratically with collagen concentration just as it does for dilute collagen gels. Following the rule that the collagen concentration of a tissue sample is 7 times greater than its hydroxyproline concentration [29], we estimate the collagen concentration in 4T1 mouse carcinoma tumors at 1-2 percent. However, the much larger collagen concentration of rat fibroadenomas appears to nullify the quadratic relationship between $C$ and $\mu$ found in carcinomas. We find in fibroadenomas that $\mu \sim C^{4.3}$. We believe changes in collagen fiber organization are responsible for the high sensitivity of fibrotic lesion stiffness to changes in collagen concentration.

Thirdly, the measured values of elastic and viscous coefficients are highly dependent on the rheological model assumed. For the same rat fibroadenoma tumors, we found $\mu = 2.6$ - 24.5 kPa and $\eta = 2.0$ - 4.0 Pa·s for the Maxwell model, and $\mu = 3.9$ - 23.3 kPa and $\eta = 2.0$ - 5.0 Pa·s for the Zener model. These values are typically larger than those obtained using the K-V model for the same dispersion curves ($\mu = 1.8$ - 4.5 kPa and $\eta = 0.9$ - 3.5 Pa·s). Since the estimated values and the between-class difference (object contrast) vary from model to model, the best model for representing breast tumor properties may not be the same as the best model for classifying tumors. The ideal estimation method is to obtain the data necessary to estimate $G'$ and $G''$ at each frequency irrespective of rheological model. For this we can use Eqs. (6) and (7) and measurements of shear-wave speed $c_s(\omega)$ and attenuation coefficient $\alpha(\omega)$:

$$c_s(\omega) = \omega/\Re\{k\} = \sqrt{\frac{2(G'^{\,2} + G''^{\,2})}{\rho(G' + \sqrt{G'^{\,2} + G''^{\,2}})}} \tag{6}$$

$$\alpha(\omega) = \Im\{k\} = \sqrt{\frac{\rho\omega^2(\sqrt{G'^{\,2} + G''^{\,2}} - G')}{2(G'^{\,2} + G''^{\,2})}}\,. \tag{7}$$

If desired, $G'(\omega)$ and $G''(\omega)$ can help to identify appropriate rheological models. For example, Eq. (3) shows that for the K-V model $G'$ (the shear storage modulus) is constant with frequency while $G''$ (the shear loss modulus) increases linearly with $\omega$. Thus, the shape of $G'(\omega)$ and $G''(\omega)$ curves can be used to identify rheological models appropriate for various tissue types.

However, model-independent estimators of $G = G' + jG''$ require estimation of the real and imaginary parts of wave number $k$; that is, we need to estimate both $\alpha$ and $c_s$. Estimates of $\alpha$ in tissues are susceptible to many measurement errors when made in small heterogeneous media like we find in tumors. Thus, we and others assume the K-V model and use Eqs. (3) and (6) to estimate $\mu$ and $\eta$ over as many frequencies as we can measure $c_s$. Is that a reasonable approach?

Since the dispersion data fit to the K-V model is poorer than the fits to the Maxwell and Zener models, why do we and others use the K-V model? One reason for the poorer fit is that K-V model does not capture the quick increase in $c_s$ often observed at vibration frequencies $<$200 Hz. The Maxwell and Zener models do capture this increase. When $\mu_2 \rightarrow \infty$, the Zener model converges to the K-V model, and when $\mu_1 \rightarrow 0$, it converges to the Maxwell model. It can easily adapt to different shape of dispersion curves thus it makes sense that it fits the dispersion data best. From Fig 7, we see that rat tumors 1 and 3 are closer to the K-V model and tumors 2 and 4 are better represented by the Maxwell model because they both have low $c_s$ value at low frequencies. This model difference is not seen in mouse carcinomas. One reason for the variations in fibroadenomas is that $c_s$ estimates at low frequencies are biased low from the reflected waves in small lesions. While in mouse carcinomas, estimates at all frequencies are biased low. Thus, one biased value of $c_s$ at low frequency could strongly influence Zener-model coefficients, and that effect increases within-class variability. Another reason for model differences is that no one model may be able to fully represent tissue measurements over the entire frequency range.

From the analysis of residuals, we could not conclude which model is most representative of these tissues. However, we note that the K-V model provides the largest between-class separability among three rheological models. That is, the ability of $\mu$ to separate fibroadenomas from carcinomas is better with K-V than other models. In the elastic model, the correlation coefficient between elasticity and collagen content is 0.85 which shows significant correlation between the two. In viscoelastic model, the elastic and viscous coefficients were both highly correlated to tumor collagen content when estimated using the K-V model (the correlation coefficient relating the two measurements is 0.95 for $\mu$ and $C$ and 0.81 for $\eta$ and $C$). The elastic modulus coefficient was highly correlated to tumor collagen content for the Maxwell model (correlation coefficient is 0.94) but not the viscous coefficient (correlation coefficient is 0.57). For the Zener model, the elastic $\mu_1 + \mu_2$ and viscous coefficients were both weakly correlated (0.85 and 0.73, respectively). The higher correlation between shear-modulus coefficients and collagen concentration for the K-V model increases parametric contrast, and this improve diagnostic performance provided that collagen concentration is a reliable biomarker for malignant phenotypes.

The best rheological model for the task of diagnosing tumors is one that generates coefficients that are reliably sensitive to tissue pathology described by the histological features that define disease. Clinical trials designed to evaluate the diagnostic performance of elasticity imaging for classifying breast lesions should include a correlation analysis between modulus coefficients and characteristic histology.

## V. CONCLUSION

Based on the discussion above, our measurements using the K-V model compare favorably with the literature, which suggests that 1) rat mammary tumor models are representative of the mechanoenviroment in human fibroadenoma tumors and provide good experimental models for studying viscoelastic contrast in elasticity imaging. 2) Shear-wave-based measurements of elastic and viscous coefficients yield consistent values with breast tumors reported by other groups regardless of species or imaging technique. 3) Large within-class variability should be subclassified into histologically-specified grades when possible to improve lesion classification. 4) The smaller the tumor size is, the lower that shear wave velocity is biased. In tissue applications, the distance from the tumor boundary is recommended to be at least one wavelength when harmonic forces are applied. 5) There is no reason why any one rheological model should best represent all of the types of breast tissues encountered clinically. Rheological models are a convenient way to reduce mechanical descriptions to a few coefficients; however, they do not describe fundamental properties because tissues form mechanical structures and are not the material continua appropriate to the models.

## ACKNOWLEDGMENT

The authors gratefully acknowledge the Brendan Harley Research Laboratory at the University of Illinois and Dan Weisgerber for guiding our collagen assays. Many thanks to Melissa Izard, who worked on the animal model and performed tissue histology. Ms. Yue Wang is a trainee funded at UIUC from NIH National Cancer Institute Alliance for Nanotechnology in Cancer Midwest Cancer Nanotechnology Training Center Grant R25 CA154015A.

## APPENDIX

Let $w_i$ be an incident plane wave of unit amplitude traveling to the left. Then $w_r$ is a reflected wave of amplitude $0 < A < 1$ from a boundary located at $x = R$ that is traveling to the right. At radial temporal $\omega$ and spatial $k$ frequencies,

$$w_i(x,t) = e^{-\alpha x} \cos(\omega t - kx)$$
$$w_r(x,t) = Ae^{-\alpha(R-x)} \cos(\omega t + kx + \phi)$$

where $A = A_0 e^{-\alpha R}$, $A_0$ and $\phi$ are reflection coefficients, and $k = 2\pi/\lambda$ is the wave number at shear wavelength $\lambda$. Assuming $w_i$ is reflected only once before it dissipates, the net wave in steady state is the sum,

$$w = w_i + w_r = \cos(\omega t + \phi/2 + \theta(x)) \, ,$$

where the spatial phase is

$$\theta(x) = \arctan\left(\frac{1 - A_0 e^{-2\alpha R(1-x/R)}}{A_0 e^{-2\alpha R(1-x/R)} + 1}\tan(-kx - \phi/2)\right) \quad \text{and } 0 \leqslant x/R, A_0 \leqslant 1 \ .$$

When $A_0 = 0$, there is no reflection from the boundary. Therefore $w = w_i$, and phase is a linear function of position from the source: $\theta(x) = -kx - \phi/2$ and $d\theta/dx = -\omega/c_s$. At the other extreme, when $A_0 = 1$ and $\alpha = 0$, then $\theta(x) = 0$ and a standing wave is generated.

## REFERENCES

[1] Deryugina EI, Quigley JP. The role of matrix metalloproteinases in cellular invasion and metastasis. In: Parks W, Mecham R, editors. Extracellular matrix degradation. Berlin: Springer-Verlag Berlin, 2011; p. 145-91.

[2] Lu P, Takai K, Weaver VM, Werb Z. Extracellular matrix degradation and remodeling in development and disease. Cold Spring Harbor Perspectives in Biology. 2011;3(12):24

[3] Mangia A, Malfettone A, Rossi R, Paradiso A, Ranieri G, Simone G, et al. Tissue remodelling in breast cancer: human mast cell tryptase as an initiator of myofibroblast differentiation. Histopathology. 2011;58(7):1096-106.

[4] Lu P, Weaver VM, Werb Z. The extracellular matrix: A dynamic niche in cancer progression. Journal of Cell Biology. 2012;196(4):395-406.

[5] Samani A, Zubovits J, Plewes D. Elastic moduli of normal and pathological human breast tissues: An inversion-technique-based investigation of 169 samples. Physics in Medicine and Biology. 2007;52(6):1565-1576.

[6] Levental KR, Yu HM, Kass L, et al. Matrix Crosslinking Forces Tumor Progression by Enhancing Integrin Signaling. Cell. 2009;139(5):891-906.

[7] Schedin P, Keely PJ. Mammary gland ECM remodeling, stiffness, and mechanosignaling in normal development and tumor progression. Cold Spring Harbor perspectives in biology. 2011;3(1).

[8] Rzymski P, Skrzewska A, Skibiska-Zieliska M, Opala T. Factors influencing breast elasticity measured by the ultrasound shear wave elastography - Preliminary results. Archives of Medical Science. 2011;7(1):127-133.

[9] Evans A, Whelehan P, Thomson K, et al. Quantitative shear wave ultrasound elastography: initial experience in solid breast masses. Breast Cancer Research. 2010;12(6).

[10] Schmitt C, Henni AH, Cloutier G. Characterization of blood clot viscoelasticity by dynamic ultrasound elastography and modeling of the rheological behavior. Journal of Biomechanics. 2011;44(4):622-629.

[11] Robert B, Sinkus R, Larrat B, Tanter M, Fink M. A new rheological model based on fractional derivatives for biological tissues. Proceeding - 2006 IEEE Ultrasonics Symposium. 2006;1033-1036.

[12] Dunn F. Temperature and amplitude dependence of acoustic absorption in tissue, J Acoust Soc Am, 1962; 34:1545-1547.

[13] Frizzell LA, Carstensena EL, Dyro JF. Shear properties of mammalian tissues at low megahertz frequencies, J Acoust Soc Am, 1976; 60:1409-1411.

[14] Insana MF, Oelze M. Advanced ultrasonic imaging techniques for breast cancer research. In: Suri JS, Rangayyan RM, Laxminarayan S, editors. Emerging Technologies in Breast Imaging and Mammography. American Scientific Publishers, Valencia CA, 2008; pp. 141-160.

[15] Falzon G, Pearson S, Murison R. Analysis of collagen fibre shape changes in breast cancer. Physics in Medicine and Biology. Dec 2008;53(23):6641-6652.

[16] Samuel CS. Determination of collagen content, concentration, and sub-types in kidney tissue. Methods Mol Biol. 2009;466:223-235.

[17] Orescanin M, Insana MF. Shear modulus estimation with vibrating needle stimulation. IEEE Trans Ultrason Ferroelect Freq Control. 2010;57(6):1358-1367.

[18] Dutt V, Kinnick RR, Muthupillai R, Oliphant TE, Ehman RL, Greenleaf JF. Acoustic shear-wave imaging using echo ultrasound compared to magnetic resonance elastography. Ultrasound Med Biol. 2000;26(3):397-403.

[19] Madsen EL, Sathoff HJ, Zagzebski JA. Ultrasonic shear wave properties of soft tissues and tissuelike materials, J Acoust Soc Am, 1983;74(5): 1346-1355.

[20] Tschoegl N. Phenomenological Theory of Linear Viscoelastic Behavior: An Introduction, Springer-Verlag, New York, 1989.

[21] Rouze NC, Wang MH, Palmeri ML, Nightingale KR. Parameters affecting the resolution and accuracy of 2-D quantitative shear wave images. IEEE Transactions on Ultrasonics Ferroelectrics and Frequency Control. 2012;59(8):1729-1740.

[22] Orescanin M, Wang Y, Insana MF. 3-D FDTD Simulation of Shear Waves for Evaluation of Complex Modulus Imaging. IEEE Transactions on Ultrasonics Ferroelectrics and Frequency Control. 2011;58 (2): 389-398.

[23] Orescanin M, Toohey K, Insana MF. Material properties from acoustic radiation force step response. J Acoust Soc Am, 2009;125:2928-2936.

[24] Okano F. Study on stromal component of mastopathy–content and type of collagen. The Hokkaido journal of medical science. 1985;60(4):555-570.

[25] Cechowska-Pasko M, Palka J, Wojtukiewicz MZ. Enhanced prolidase activity and decreased collagen content in breast cancer tissue. International Journal of Experimental Pathology. 2006;87(4):289-296.

[26] Sridhar M, Liu, J, Insana MF. Viscoelasticity imaging using ultrasound: parameters and error analysis. Phys Med Biol, 2007;52:2425-2443.

[27] Sinkus R, Tanter M, Xydeas T, Catheline S, Bercoff J, Fink M. Viscoelastic shear properties of in vivo breast lesions measured by MR elastography. Magnetic Resonance Imaging. 2005;23(2):159-165.

[28] Orescanin M, Qayyum MA, Toohey KS, Insana MF. Dispersion and shear modulus measurements of porcine liver. Ultrasonic Imaging, 2010; 32, 255-266.

[29] Cheng W, Yan-Hua R, Fang-Gang N, Guo-An Z. The content and ratio of type I and III collagen in skin differ with age and injury. African Journal of Biotechnology. 2011;10(13):2524-2529.

[30] Barnes SL, Young PP, Miga MI. A novel model-gel-tissue assay analysis for comparing tumor elastic properties to collagen content. Biomechanics and Modeling in Mechanobiology. 2009;8(4):337-43.

[31] Yang YL, Leone LM, Kaufman LJ. Elastic Moduli of Collagen Gels Can Be Predicted from Two-Dimensional Confocal Microscopy. Biophysical Journal. 2009;97(7):2051-60.